LETTER

Maximal Rashba-like spin splitting via kinetic-energy-coupled inversion-symmetry breaking

Veronika Sunko[1,2], H. Rosner[2], P. Kushwaha[2], S. Khim[2], F. Mazzola[1], L. Bawden[1], O. J. Clark[1], J. M. Riley[1,3], D. Kasinathan[2], M. W. Haverkort[2,4], T. K. Kim[3], M. Hoesch[3], J. Fujii[5], I. Vobornik[5], A. P. Mackenzie[1,2] & P. D. C. King[1]

Engineering and enhancing the breaking of inversion symmetry in solids—that is, allowing electrons to differentiate between 'up' and 'down'—is a key goal in condensed-matter physics and materials science because it can be used to stabilize states that are of fundamental interest and also have potential practical applications. Examples include improved ferroelectrics for memory devices and materials that host Majorana zero modes for quantum computing[1,2]. Although inversion symmetry is naturally broken in several crystalline environments, such as at surfaces and interfaces, maximizing the influence of this effect on the electronic states of interest remains a challenge. Here we present a mechanism for realizing a much larger coupling of inversion-symmetry breaking to itinerant surface electrons than is typically achieved. The key element is a pronounced asymmetry of surface hopping energies—that is, a kinetic-energy-coupled inversion-symmetry breaking, the energy scale of which is a substantial fraction of the bandwidth. Using spin- and angle-resolved photoemission spectroscopy, we demonstrate that such a strong inversion-symmetry breaking, when combined with spin–orbit interactions, can mediate Rashba-like[3,4] spin splittings that are much larger than would typically be expected. The energy scale of the inversion-symmetry breaking that we achieve is so large that the spin splitting in the CoO_2- and RhO_2-derived surface states of delafossite oxides becomes controlled by the full atomic spin–orbit coupling of the $3d$ and $4d$ transition metals, resulting in some of the largest known Rashba-like[3,4] spin splittings. The core structural building blocks that facilitate the bandwidth-scaled inversion-symmetry breaking are common to numerous materials. Our findings therefore provide opportunities for creating spin-textured states and suggest routes to interfacial control of inversion-symmetry breaking in designer heterostructures of oxides and other material classes.

The natural breaking of inversion symmetry at surfaces and interfaces provides a way of stabilizing electronic structures that are distinct from those of the bulk[4,5]. A notable example is found in materials that also have strong spin–orbit interactions, in which inversion-symmetry breaking (ISB) underpins Rashba[3,4] spin splitting of surface- or interface-localized two-dimensional electron gases[6–11], which are generically characterized by a locking of the quasiparticle spin perpendicular to its momentum. Such effects are central to various applications that have been proposed in spin-based electronics and provide routes to stabilizing new physical regimes[4,12–15]. Conventional wisdom about the way in which to maximize the Rashba effect has been to work with heavy elements with large atomic spin–orbit coupling (SOC). However, the energetic spin splittings that are obtained are usually only a small fraction of the atomic spin–orbit energy scale. This is because the key physics is not exclusively that of SOC, but rather an interplay between the spin–orbit (E_{SOC}) and inversion-breaking (E_{ISB}) energy scales.

Evidencing the importance of this interplay, the size of the spin splitting can often be controlled by tuning the strength of the ISB potential, for example, via applied electrostatic gate voltages[7]. This sensitivity to E_{ISB} indicates a regime in which the achievable spin splitting is limited by E_{ISB}, typically to only a modest percentage of the atomic SOC (Fig. 1a)[16–18]. If, however, an ISB energy scale can be achieved that is much larger than that of the SOC, then the spin–orbit Hamiltonian will act as a perturbation to a Hamiltonian dominated by the ISB. A fourfold-degenerate level will be split by ISB into two states of opposite orbital angular momentum (OAM). The weaker spin–orbit interaction cannot mix these states and instead further spin-splits them into states of spin that are parallel and antiparallel to the pre-existing OAM, with a splitting that must therefore take the full atomic SOC value (Fig. 1b)[16–18]. This limit is clearly desirable for maximizing the achievable spin splitting for a given strength of SOC, but is typically realized only when the absolute value of SOC, and consequently also the total spin splitting, is small.

Here we demonstrate a method for using the intrinsic energetics of hopping to realize large ISB energy scales at the surfaces of transition-metal-based delafossite oxides $(Pd,Pt)(Co,Rh)O_2$. We show, from spin- and angle-resolved photoemission (ARPES), that this large
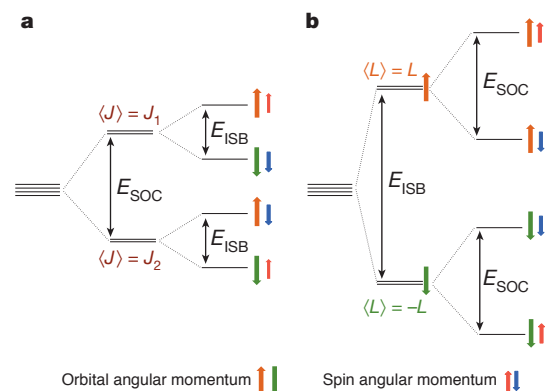

Figure 1 | Interplay between two energy scales for realizing spin splitting in inversion-asymmetric environments. Schematic illustration of how a fourfold-degenerate state becomes split by ISB and SOC. **a**, Dominant SOC first forms states of defined total angular momentum J, split by the atomic SOC (E_{SOC}), and with the orbital (OAM) and spin (SAM) angular momentum locked to each other. ISB splits them additionally into states of opposite spin, separated by E_{ISB}. **b**, If E_{ISB} dominates, the initial splitting is between states of opposite OAM. The weaker SOC cannot mix the states that are split by ISB and so introduces splitting between the states of spin that are parallel and antiparallel to the preexisting OAM, with a magnitude of the order of E_{SOC}. For a given SOC strength, the spin splitting is therefore largest if $E_{ISB} \gg E_{SOC}$.

[1]SUPA, School of Physics and Astronomy, University of St Andrews, St Andrews KY16 9SS, UK. [2]Max Planck Institute for Chemical Physics of Solids, Nöthnitzer Straße 40, 01187 Dresden, Germany. [3]Diamond Light Source, Harwell Campus, Didcot OX11 0DE, UK. [4]Institute for Theoretical Physics, Heidelberg University, Philosophenweg 19, 69120 Heidelberg, Germany. [5]Istituto Officina dei Materiali (IOM)-CNR, Laboratorio TASC, Area Science Park, S.S.14, Km 163.5, 34149 Trieste, Italy.
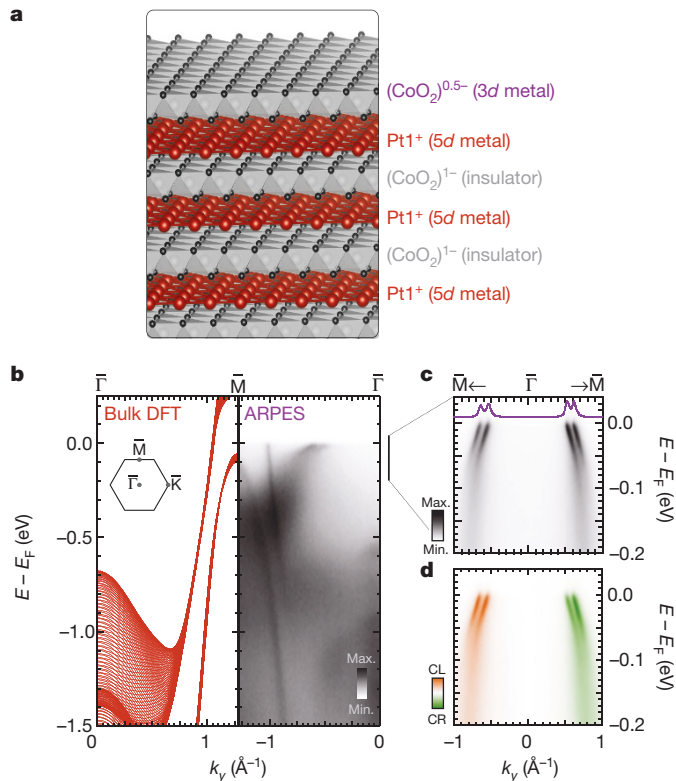
however, the 'missing' Pt atoms from above the topmost oxygen layer cause the CoO_2 block to have a formal valence of only 0.5^-, effectively hole-doping the manifold of Co-derived states[23]. Consistent with this simple ionic picture, our ARPES data not only show sharp and rapidly dispersing spectral features that are representative of the bulk band structure[22], but also a pair of two-dimensional hole bands that cross the Fermi level where none are expected from the calculated bulk electronic structure at any value of the out-of-plane momentum, k_z (Fig. 2b and Extended Data Fig. 1a).

The inner and outer bands form almost circular and hexagonally warped hole-like Fermi surfaces located at the Brillouin zone centre (Fig. 3a). Their Luttinger count is approximately 0.4 holes per unit cell, very close to the 0.5 holes that would be expected from simple electron counting. This therefore seems like a remarkably clean example of an 'electronic reconstruction', a phenomenon that has been discussed extensively for polar transition-metal oxide interfaces[5]. The bands that we observe host heavy quasiparticles with masses of up to around $15m_e$, where m_e is the free-electron mass (see Extended Data Table 1 for a more detailed description of the quasiparticle masses and their anisotropy) and have clear spectroscopic signatures of electron–phonon and electron–electron interactions (Fig. 2b, c). This is in stark contrast to the almost free-electron masses of the bulk Pt-derived bands that cross the Fermi energy E_F (ref. 22), and suggests that these states are instead predominantly derived from much more local Co 3d orbitals. Consistent with this, we note that similar dispersions have previously been observed[24] in the sister compound $PdCoO_2$. We therefore identify these bands as surface states of the CoO_2-terminated surface of $PtCoO_2$, with very little intermixing of Pt; this is further confirmed by our density functional theory (DFT) calculations, described below.

Our ARPES measurements performed using circularly left- and circularly right-polarized light reveal a strong circular dichroism (CD) of these surface states (Fig. 2d and Extended Data Fig. 1). CD–ARPES is known to be sensitive to OAM structures in solids[25]. Whereas OAM would naturally be expected to be quenched for the t_{2g} manifold, the observation of a pronounced circular dichroism across the entire bandwidth of the surface states here suggests that these instead host a large OAM. Moreover, from spin-resolved ARPES measurements (Fig. 3c; see Methods) we find that the two surface states are strongly spin-polarized, with a large in-plane spin component that points perpendicular to their momentum. This finding indicates chiral spin textures of the form that would be expected for a Rashba-like splitting[3]. Whereas the spin chirality reverses sign between the inner and outer Fermi surface sheets, the circular dichroism of each spin-split branch is of the same sign (Fig. 2d and Extended Data Fig. 1). This suggests that both branches carry the same sign of OAM, with spin splitting resulting from the parallel and antiparallel alignment of the spin to this OAM, in close agreement with the situation shown in Fig. 1b. Critically, this spin and OAM texture should lead to a spin splitting that is of the order of the full strength of atomic SOC.

Our DFT supercell calculations fully support the above analysis. They confirm that the surface states host dominantly chiral spin angular momentum (orbital angular momentum) textures, which are of the opposite (same) sign for the two surface Fermi surfaces (Fig. 3b, d; see also Extended Data Fig. 2). Moreover, the calculations reveal that these states host a spin splitting that remains large over the entire bandwidth of the states, except near time-reversal-invariant momenta ($\overline{\Gamma}$ and $\overline{M}$), at which time-reversal symmetry dictates that it must vanish. Away from these points, the spin splitting reaches values as high as 60 meV at the average Fermi wavevector k_F along the $\overline{\Gamma}$–$\overline{K}$ direction. This is comparable to the atomic SOC strength of Co (ref. 26). A surface projection of our calculations (Fig. 3e) indicates that the wavefunctions of the surface states are almost entirely located in the topmost CoO_2 block; they therefore exhibit a spin splitting that is indeed of the maximum strength possible for the relevant Co atomic orbitals.

Figure 2 | Bulk and surface electronic structure of $PtCoO_2$. a, The layered $PtCoO_2$ delafossite structure, with linearly coordinated metallic Pt (formal charge of 1+) layers separated by layers of $(CoO_2)^{1-}$ octahedra. Such ionic structure suggests a metallic $(CoO_2)^{0.5-}$ surface. **b, c,** Both k_z-projected bulk density functional theory (DFT) calculations (left in **b**) and an ARPES measurement (right in **b**; photon energy $h\nu = 88$ eV, s-polarized light) of the electronic structure along the $\overline{\Gamma}$–$\overline{M}$ direction of the surface Brillouin zone reveal a two-dimensional band that crosses the Fermi level and a fully occupied hole band centred at the $\overline{M}$ point. Two additional hole-like bands that cross the Fermi level are evident in **b**, shown magnified in **c** for measurement conditions ($h\nu = 100$ eV, p-polarized light) that increase their spectral weight. We attribute these to surface states of the top CoO_2 layer. These bands have 'kinks' close to the Fermi level, and increased broadening away from the Fermi energy E_F, which are characteristic spectroscopic signatures of many-body interactions. Momentum distribution curves at the Fermi level ($E_F \pm 5$ meV) are shown by the purple lines. **d,** Experimental circular dichroism measurements ($h\nu = 100$ eV) suggest that these surface states host a strong OAM, of the same sign for each surface-state branch. CL and CR denote circular-left and circular-right polarisation, respectively; $E - E_F$ is the electon energy referenced to the Fermi energy; and k_y is the in-plane momentum along the $\overline{\Gamma}$–$\overline{M}$ direction.

energy scale leads to spin-split Fermi surfaces with one of the largest momentum separations known, even for the unlikely environment of a 3d-electron-based CoO_2 metal, where atomic SOC is not strong. Crucially, we demonstrate that E_{ISB} scales with the bandwidth and so will grow concomitant with the SOC strength upon moving to systems of heavier elements. We show that this scaling enables the full atomic SOC to be retained in spin-splitting the states of a 4d RhO_2 surface layer, leading to an unprecedented spin splitting for an oxide compound of approximately 150 meV, and providing new opportunities for tuning between giant spin splittings and strongly interacting Rashba-like states in oxides and other compounds.

We first consider the delafossite oxide[19–21] $PtCoO_2$. Pt^{1+} cations sit on a triangular lattice, leading to extremely high bulk conductivity[22], and are separated by layers of edge-sharing and trigonally distorted cobalt oxide octahedra (Fig. 2a). In the bulk, six 3d electrons fill the Co t_{2g} manifold, which makes the CoO_2 block insulating. At the surface,
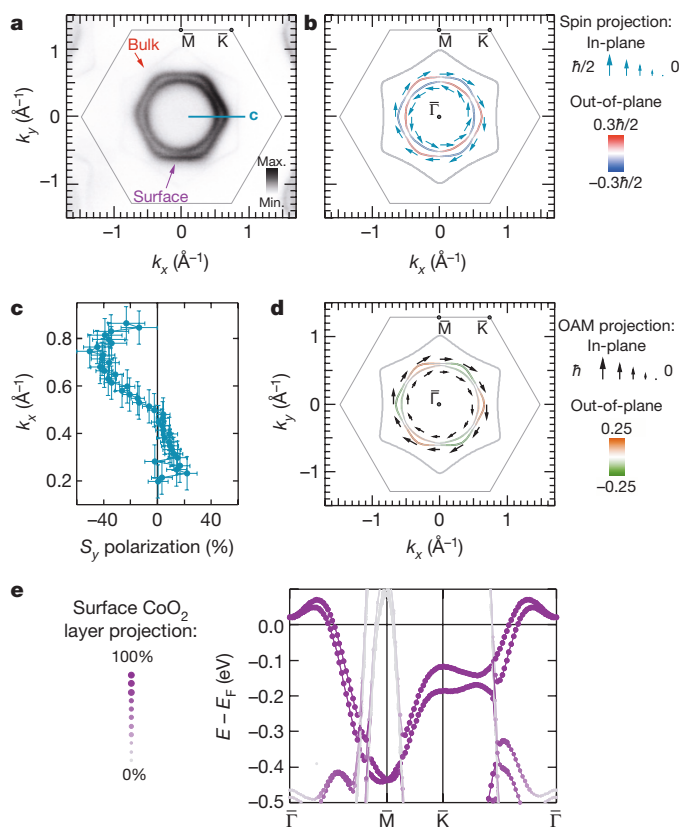
Figure 3 | Spin-polarized surface states. a, b, Bulk and surface Fermi surfaces of $PtCoO_2$ (**a**) measured by ARPES (**a**; $E_F \pm 5$ meV, $h\nu = 110$ eV, p-polarized light) and from a CoO_2-terminated DFT supercell calculation (**b**, grey lines). k_x and k_y are the in-plane crystal momenta in the $\overline{\Gamma}-\overline{K}$ and $\overline{\Gamma}-\overline{M}$ directions, respectively. The colour scale in **a** represents the photoemission intensity. Spurious bulk hole pockets near $\overline{M}$ from the calculations are not shown (see Methods). **c**, Spin-resolved ARPES measurements ($h\nu = 65$ eV, p-polarized light) of an in-plane spin polarization ($\langle S_y \rangle$) of the Fermi surface for the cut along k_x shown in **a**. Error bars reflect an estimate of the uncertainty in extracting the spin polarization from the experimental measurements as a function of in-plane momentum, incorporating statistical and systematic errors. These measurements reveal a Rashba-like spin texture of the surface states. This spin texture is supported by our supercell calculations (**b**), which show a chiral in-plane spin texture as well as some out-of-plane spin canting. The length of the arrows in **b** encodes the modulus of the expectation value of spin along a quantization axis perpendicular to the in-plane momentum; the expectation value parallel to the momentum direction is zero. The expected value of the out-of-plane spin ($\langle S_z \rangle$) is shown by the colour. **d**, The calculated OAM (see Methods) is of the same sign on the two spin-split branches, consistent with the schematic shown in Fig. 1b. **e**, Electronic structure from the DFT supercell calculations projected onto the first CoO_2 layer, demonstrating that the bands that make up these Fermi surfaces have almost all of their wavefunction weight on the surface CoO_2 block.

Spin–orbit interactions are generally neglected for such $3d$-orbital systems. In contrast, Figs 1–3 demonstrate that these interactions can lead to a major restructuring of the electronic structure if a sufficiently strong ISB can be realized to unlock their full strength, opening up the potential for investigating the interplay between spin–orbit interactions and strong electronic correlations, the latter being more naturally associated with local $3d$ orbitals. For the CoO_2-terminated surface of $PtCoO_2$, achieving the maximum possible energetic spin splitting as well as high quasiparticle masses leads to momentum spin splittings at the Fermi level (the relevant quantity for several technological applications) as high as $\Delta k_F = 0.13 \pm 0.01$ Å^{-1} (see also Extended Data Table 1). This value is among the highest known for

any Rashba-like system[27]. It is approximately ten times larger than that of the enhanced Rashba-like splitting that is thought to occur at isolated momentum points where different t_{2g} bands intersect in the $3d$-orbital system of $SrTiO_3$-based two-dimensional electron gases[10,28–30], and is comparable in magnitude to the momentum splitting in the so-called giant Rashba semiconductor BiTeI (refs 27, 31), which has both very strong SOC and large internal electrostatic potential gradients. We note that our experimentally observed Fermi surfaces (Fig. 3a) are well reproduced by our DFT calculations, which consider an ideal bulk-truncated supercell. This rules out subtle modulations in surface structure, such as those known to markedly enhance Rashba spin splitting in various surface alloy systems[9,32], as the origin of the large effects observed here. Instead, the agreement between theory and experiment identifies the spin splitting that we observe as an intrinsic property of the bulk-like CoO_2 layer, which is unlocked when it is placed in an environment in which inversion symmetry is broken by the presence of the surface.

We now show that the surprisingly large spin splitting occurs as a natural consequence of a strong asymmetry in effective Co–Co hopping paths through oxygen atoms located above and below the topmost Co layer. The structure of a single CoO_2 layer is shown in Fig. 4a, b. This structure can be viewed as a trilayer unit, with a central triangular net of Co atoms, above and below which are two triangular oxygen sublattices that have opposite orientation with respect to Co. Given the local nature of $3d$ orbitals, an important effective Co–Co hopping will be via oxygen, either through the oxygen layer above (O1) or below (O2) the transition-metal plane. In bulk, these effective hoppings must be equivalent owing to the inversion symmetry of the crystal structure. However, this requirement is lifted at the surface. To demonstrate this explicitly, we show in Fig. 4c the projection of the electronic structure from our DFT supercell calculations onto O1 and O2 of the surface CoO_2 layer. It is clear that there is a much higher admixture of O1 than O2 in the CoO_2-derived surface states that intersect the Fermi level identified above: we estimate that the O1 orbital contribution is approximately 2.4 times higher than that of O2 when averaged around the surface Fermi surfaces. This indicates that Co–O–Co hopping occurs dominantly via the oxygen network above, rather than below, the transition-metal plane in the surface CoO_2 layer.

The microscopic origin of the hopping being predominantly via O1 is evident from the layer-projected oxygen partial density of states (PDOS) shown in Fig. 4d. Although the PDOS of O2 is similar to those of subsequent layers of our supercell calculation, that of O1 is strongly shifted in energy, with the main centroid of spectral weight located at a binding energy that is approximately 4 eV lower than that of O2 (see also Extended Data Fig. 3a, b). In the bulk[22], and in the bulk-like environment of O2, the bonding Pt–O combinations shift the predominantly oxygen-derived levels to higher binding energy. An absence of this shift as a result of the missing Pt above O1 therefore causes the difference in on-site energy of the two oxygen atoms. In a tight-binding picture, Co–O–Co hopping via On ($n = 1, 2$) is described by the effective transfer integral, $t_n = t_{dp}^2/(E_{Co} - E_{On})$ where t_{dp} is the Co $3d$–O $2p$ hopping matrix element (Fig. 4a) and E_{Co} and E_{On} are the on-site energies of Co and On (Fig. 4e). The decrease in binding energy of the oxygen-derived PDOS on site 1 leads to a strongly asymmetric hopping with $t_1 > t_2$ and thus directly to a large E_{ISB}.

To validate that this asymmetry drives the spin splitting observed here, we develop a minimal tight-binding model for a single CoO_2 layer (see Methods and Extended Data Fig. 4). This model yields an estimate of the relative ISB that is introduced by the asymmetric hopping of $\alpha_{ISB} = (t_1 - t_2)/(t_1 + t_2) > 40\%$. The asymmetry enters between two hopping paths, which are nominally equivalent in bulk and which define the entire bandwidth; the energy scale of the ISB is therefore large: $E_{ISB} = \alpha_{ISB}t \approx 150$ meV, where t is the average effective Co–O–Co hopping integral. This energy scale is approximately twice the atomic SOC and so places the CoO_2 surface within the 'strong ISB' limit discussed above (Fig. 1b; see also Extended Data Fig. 5),
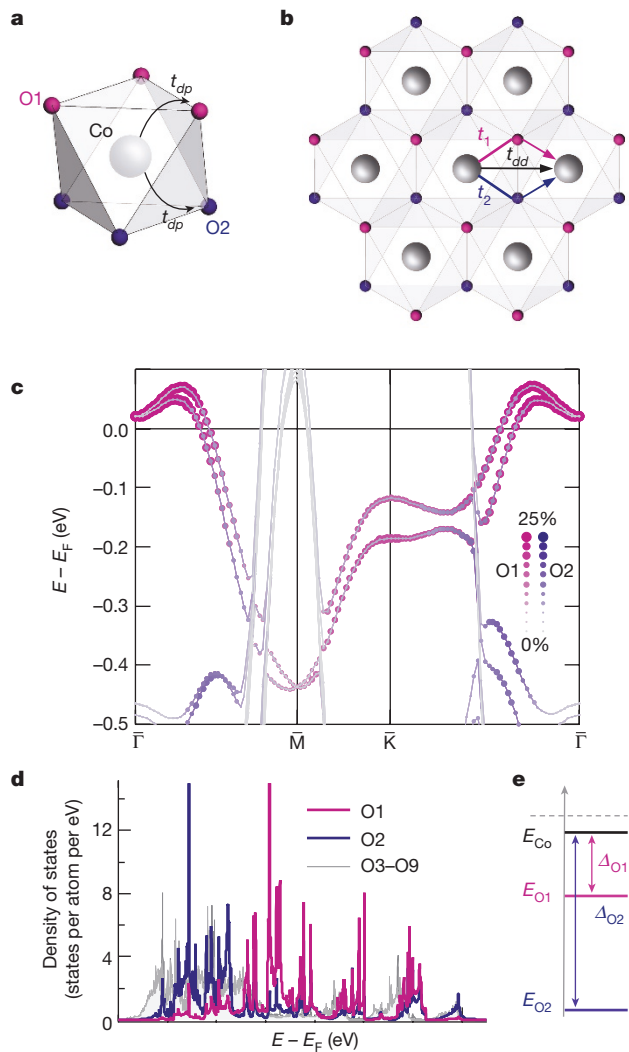
Figure 4 | Origin of the spin splitting. a, A single Co–O octahedron. The hopping integral between Co and O in layers above (O1, pink) and below (O2, purple) the Co is denoted t_{dp}. **b**, Top view of the surface CoO_2 layer. As shown schematically, an electron can hop between two Co atoms either directly (t_{dd}) or via the O atoms (effective hopping integrals t_1 and t_2, for O1 and O2, respectively). **c**, DFT supercell band-structure calculations, projected onto O1 (pink) and O2 (purple), revealing that the dominant contribution to the surface states is from O1. **d, e**, The layer-resolved oxygen partial density of states (PDOS; **d**) indicates that the dominant contribution from O1 arises as a result of a shift of about 4 eV to lower binding energy of the PDOS of O1 with respect to that of O2, represented schematically as an on-site energy shift (**e**). The PDOS of O2 is similar to that of the bulk-like oxygen atoms in deeper layers (O3–O9, grey lines in **d**). Δ_{O1} (Δ_{O2}) are the on-site energy differences between Co and O1 (O2).

Figure 5 | Bandwidth-scaled inversion-symmetry breaking. a, c, e, Spin-split surface states of $PtCoO_2$ (**a**), $PdCoO_2$ (**c**) and $PdRhO_2$ (**e**), indicating a spin splitting that scales with the SOC strength of the B-site transition metal ($PdCoO_2$ (**c**) versus $PdRhO_2$ (**e**)), but is independent of the A-site metal ($PtCoO_2$ (**a**) versus $PdCoO_2$ (**c**)). The inset in **c** shows the first two Brillouin zones, with the purple line indicating the direction along which the measurements in **a, c** and **e** were taken. $k_\parallel$ is the value of in-plane crystal momentum along this direction and $k_{\overline{K}}$ the momentum at the $\overline{K}$ point. The splitting retains the strength of the atomic SOC of the transition metal even as this strength is increased by a factor of approximately 2.5 on moving from Co to Rh. This is particularly evident from the spin splitting at the $\overline{K}$ point (dashed lines in **a, c** and **e**), which is clearly visible in the energy distribution curves shown in **b, d** and **f** for $k_\parallel/k_{\overline{K}} = 1 \pm 0.05$. The arrows in **b, d** and **f** show the size of the spin splitting.

explaining why the spin splitting is so large for the Co-derived states that are observed here.

The critical feature of our analysis is that ISB need not be a weak perturbation to the Hamiltonian of the surface conduction electrons, but can enter through the kinetic part of that Hamiltonian directly. This differs substantially from previous treatments, which typically consider a dipole term arising from the surface electric field directly as the dominant symmetry breaking[16], allowing only a weak perturbation to a Hamiltonian governed by the kinetic energy[30]. We illustrate the importance of structure in achieving this kinetic-energy-coupled symmetry breaking with a simple analysis, shown in Extended Data Fig. 6, of the difference between a two-dimensional layer of edge-sharing transition-metal octahedra and the corner-sharing octahedra of, for example,
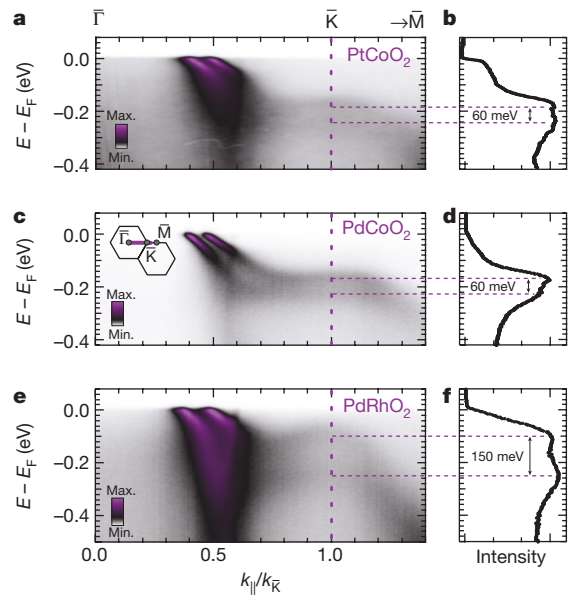
many cuprates and other transition-metal oxides[29,30]. The edge-sharing geometry of the delafossites yields an ISB that is not only strong, but is also scaled by the conduction electron bandwidth. This result suggests strategies for maximizing spin-splitting in solids that are counter to conventional wisdom: instead of just increasing the SOC, which would normally lead to the achievable spin splitting becoming limited by E_{ISB} (Fig. 1a and Extended Data Fig. 5), the 'bandwidth-scaled' E_{ISB} will simultaneously grow with increased orbital overlap of heavy-element systems, enabling the maximum possible spin splittings to be retained even in systems with much stronger SOC.

To verify the potential of this new approach, it is desirable to perform two further experiments. The first is to compare the surface states of $PtCoO_2$ with those of $PdCoO_2$ in order to rule out an influence of the strong SOC of the noble-metal cation in mediating our observed spin splittings. The second is to change the transition metal from Co to Rh, to test whether the spin splitting really scales with the factor of approximately 2.5 increase of transition-metal SOC. The former is easy to do, because high-quality $PdCoO_2$ crystals are straightforward to synthesize[20]. However, $PdRhO_2$, although known to be metallic in polycrystalline form[19], has not to our knowledge previously been synthesized in single-crystal form. We did so for this project.

As shown in Fig. 5a, c and Extended Data Table 1, the surface-state spin splitting of $PdCoO_2$ is in good quantitative agreement with that of $PtCoO_2$. This confirms that the spin splitting that we observe is a property of the CoO_2 block, with only minimal influence from the A-site (Pd,Pt) cation. We can clearly resolve the spin-split bands across their bandwidth, extracting a spin splitting of 60 meV at the $\overline{K}$ point for both compounds (Fig. 5b, d). As shown in our tight-binding model (Extended Data Fig. 4a, b), a fourfold-degenerate band crossing would be expected at this momentum point in the absence of ISB and SOC.

It is therefore an ideal location to probe the energy scale of the spin splitting.

Our measurements of $PdRhO_2$ (Fig. 5e) reveal qualitatively similar surface states. However, the momentum splitting at the Fermi level is higher, reaching $\Delta k_F = 0.16 \pm 0.01$ Å^{-1} along $\overline{\Gamma}-\overline{K}$, despite its lower quasiparticle masses (see also Extended Data Table 1). This is a result of a strongly enhanced energetic splitting, which we find to be 150 meV at the $\overline{K}$ point (Fig. 5f). To the best of our knowledge, this is by far the largest spin splitting to be observed in an oxide so far. More importantly, it is of the order of the full atomic SOC strength of Rh^{3+} (ref. 26). The bandwidth scaling of E_{ISB} allows $PdRhO_2$ to remain in a limit in which $E_{ISB} > E_{SOC}$ even as the latter is markedly increased. This limit is further evidenced by our CD–ARPES measurements (Extended Data Fig. 1e, f), which demonstrate that both of the spin-split branches retain the same sign of OAM, as in $(Pt,Pd)CoO_2$.

This key result—that the symmetry breaking that enters into the kinetic part of the Hamiltonian directly can lead to a bandwidth-scaled E_{ISB}—is potentially realizable in any system in which hopping between the frontier orbitals is mediated by atoms above and below their plane, including the large and varied family of delafossites[21] as well as, for example, (111)-oriented surfaces and interfaces of perovskites. Immediate quantitative insight into the levels of ISB that are expected could in principle be obtained from DFT calculations, providing a reliable predictive capability of the 'materials by design' approach that is currently generating large interest from specialists in first-principles electronic structure calculations. Moreover, suitable mismatched interfaces could be fabricated by highly controlled thin-film and multilayer techniques such as molecular-beam epitaxy, providing ways to access new physical regimes.

1. Lee, H. N., Christen, H. M., Chisholm, M. F., Rouleau, C. M. & Lowndes, D. H. Strong polarization enhancement in asymmetric three-component ferroelectric superlattices. *Nature* **433**, 395–399 (2005).
2. Mourik, V. *et al.* Signatures of Majorana fermions in hybrid superconductor-semiconductor nanowire devices. *Science* **336**, 1003–1007 (2012).
3. Bychkov, Y. A. & Rashba, E. I. Properties of a 2d electron gas with lifted spectral degeneracy. *JETP Lett.* **39**, 78–81 (1984).
4. Manchon, A., Koo, H. C., Nitta, J., Frolov, S. M. & Duine, R. A. New perspectives for Rashba spin–orbit coupling. *Nat. Mater.* **14**, 871–882 (2015).
5. Hwang, H. Y. *et al.* Emergent phenomena at oxide interfaces. *Nat. Mater.* **11**, 103–113 (2012).
6. LaShell, S., McDougall, B. A. & Jensen, E. Spin splitting of an Au(111) surface state band observed with angle resolved photoelectron spectroscopy. *Phys. Rev. Lett.* **77**, 3419–3422 (1996).
7. Nitta, J., Akazaki, T., Takayanagi, H. & Enoki, T. Gate control of spin–orbit interaction in an inverted $In_{0.53}Ga_{0.47}As/In_{0.52}Al_{0.48}As$ heterostructure. *Phys. Rev. Lett.* **78**, 1335–1338 (1997).
8. Hoesch, M. *et al.* Spin structure of the Shockley surface state on Au(111). *Phys. Rev. B* **69**, 241401 (2004).
9. Ast, C. R. *et al.* Giant spin splitting through surface alloying. *Phys. Rev. Lett.* **98**, 186807 (2007).
10. Caviglia, A. D. *et al.* Tunable Rashba spin–orbit interaction at oxide interfaces. *Phys. Rev. Lett.* **104**, 126803 (2010).
11. King, P. D. C. *et al.* Large tunable Rashba spin splitting of a two-dimensional electron gas in Bi_2Se_3. *Phys. Rev. Lett.* **107**, 096802 (2011).
12. Lesne, E. *et al.* Highly efficient and tunable spin-to-charge conversion through Rashba coupling at oxide interfaces. *Nat. Mater.* **15**, 1261–1266 (2016).
13. Chesi, S. & Loss, D. RKKY interaction in a disordered two-dimensional electron gas with Rashba and Dresselhaus spin–orbit couplings. *Phys. Rev. B* **82**, 165303 (2010).
14. Grimaldi, C. Weak-and strong-coupling limits of the two-dimensional Frohlich polaron with spin–orbit Rashba interaction. *Phys. Rev. B* **77**, 024306 (2008).
15. Gor'kov, L. P. & Rashba, E. I. Superconducting 2D system with lifted spin degeneracy: mixed singlet-triplet state. *Phys. Rev. Lett.* **87**, 037004 (2001).
16. Hong, J., Rhim, J.-W., Kim, C., Ryong Park, S. & Hoon Shim, J. Quantitative analysis on electric dipole energy in Rashba band splitting. *Sci. Rep.* **5**, 13488 (2015).
17. Park, S. R. & Kim, C. Microscopic mechanism for the Rashba spin-band splitting: perspective from formation of local orbital angular momentum. *J. Electron Spectrosc. Relat. Phenom.* **201**, 6–17 (2015).
18. Park, S. R., Kim, C. H., Yu, J., Han, J. H. & Kim, C. Orbital-angular-momentum based origin of Rashba-type surface band splitting. *Phys. Rev. Lett.* **107**, 156803 (2011).
19. Shannon, R. D., Rogers, D. B. & Prewitt, C. T. Chemistry of noble metal oxides. I. Syntheses and properties of ABO_2 delafossite compounds. *Inorg. Chem.* **10**, 713–718 (1971).
20. Takatsu, H. *et al.* Roles of high-frequency optical phonons in the physical properties of the conductive delafossite $PdCoO_2$. *J. Phys. Soc. Jpn.* **76**, 104701 (2007).
21. Mackenzie, A. P. The properties of ultrapure delafossite metals. *Rep. Prog. Phys.* **80**, 032501 (2017).
22. Kushwaha, P. *et al.* Nearly free electrons in a 5d delafossite oxide metal. *Sci. Adv.* **1**, e1500692 (2015).
23. Kim, K., Choi, H. C. & Min, B. I. Fermi surface and surface electronic structure of delafossite $PdCoO_2$. *Phys. Rev. B* **80**, 035116 (2009).
24. Noh, H.-J. *et al.* Anisotropic electric conductivity of delafossite $PdCoO_2$ studied by angle-resolved photoemission spectroscopy. *Phys. Rev. Lett.* **102**, 256404 (2009).
25. Park, S. R. *et al.* Chiral orbital-angular momentum in the surface states of Bi_2Se_3. *Phys. Rev. Lett.* **108**, 046805 (2012).
26. Haverkort, M. W. *Spin and Orbital Degrees of Freedom in Transition Metal Oxides and Oxide Thin Films Studied by Soft X-Ray Absorption Spectroscopy.* PhD thesis, Univ. Cologne, http://kups.ub.uni-koeln.de/1455/ (2005).
27. Ishizaka, K. *et al.* Giant Rashba-type spin splitting in bulk BiTeI. *Nat. Mater.* **10**, 521–526 (2011).
28. King, P. D. C. *et al.* Quasiparticle dynamics and spin–orbital texture of the $SrTiO_3$ two-dimensional electron gas. *Nat. Commun.* **5**, 3414 (2014).
29. Zhong, Z., Tóth, A. & Held, K. Theory of spin–orbit coupling at $LaAlO_3/SrTiO_3$ interfaces and $SrTiO_3$ surfaces. *Phys. Rev. B* **87**, 161102 (2013).
30. Khalsa, G., Lee, B. & MacDonald, A. H. Theory of t_{2g} electron-gas Rashba interactions. *Phys. Rev. B* **88**, 041302 (2013).
31. Bawden, L. *et al.* Hierarchical spin–orbital polarization of a giant Rashba system. *Sci. Adv.* **1**, e1500495 (2015).
32. Bihlmayer, G., Blügel, S. & Chulkov, E. V. Enhanced Rashba spin–orbit splitting in Bi/Ag(111) and Pb/Ag(111) surface alloys from first principles. *Phys. Rev. B* **75**, 195414 (2007).

Author Contributions V.S., F.M., L.B., O.J.C., J.M.R. and P.D.C.K. measured the experimental data, and V.S. performed the data analysis. P.K and S.K. grew and characterized the samples. V.S. developed the tight-binding models, and H.R., D.K. and M.W.H. performed the first-principles calculations. M.H. and T.K.K. maintained the ARPES end station and J.F. and I.V. the spin-ARPES end station, and all provided experimental support. V.S., P.D.C.K. and A.P.M. wrote the manuscript with input and discussion from co-authors, and were responsible for overall project planning and direction.

METHODS

ARPES. Single-crystal samples of the delafossite oxides[19–22,33–35] $PtCoO_2$, $PdCoO_2$ and $PdRhO_2$ were grown by flux and vapour transport techniques in sealed quartz tubes. They were cleaved *in situ* at the measurement temperature of 6–10 K. (Pt,Pd)- and (Co,Rh)O_2-terminated surfaces would both be expected for a typical cleaved surface. A-site-terminated surface states have been reported previously[36] for the sister compound $PdCrO_2$, and for some cleaves we observe states that we tentatively assign as derived from Pt/Pd terminations. However, in agreement with previous studies[24], our ARPES spectra often show spectroscopic signatures arising from only the bulk and the CoO_2-terminated surface, which is the case for all of the data included here. ARPES measurements were performing using the I05 beamline of Diamond Light Source, UK. Measurements were performed using s-, p- and circularly polarized synchrotron light from 55 eV to 110 eV and using a Scienta R4000 hemispherical electron analyser. Spin-resolved ARPES measurements were performed using p-polarized synchrotron light at the APE beamline of the Elettra synchrotron[37], using a Scienta DA30 hemispherical analyser equipped with a very low-energy electron diffraction (V-LEED)-based spin polarimeter probing the spin polarization perpendicular to the analyser slit, $\langle S_y \rangle$. The finite spin-detection efficiency was corrected using a Sherman function ($S = 0.3$), determined by comparison with the known spin polarization of the Rashba-split surface states measured on the Au(111) surface. The spin polarization along momentum distribution curves at the Fermi level is extracted as

$$P = \frac{I^+ - I^-}{S(I^+ + I^-)}$$

where I^+ (I^-) is the V-LEED channeltron intensity measured along momentum distribution curves for the target magnetization polarized in the positive (negative) direction, defined with respect to the DFT calculation.

Density functional theory. Relativistic DFT electronic structure calculations were performed using the full-potential FPLO code[38,39], version fplo14.00-47 (http://www.fplo.de). The exchange correlation potential was treated within the general gradient approximation (GGA), using the Perdew–Burke–Ernzerhof[40] parameterization. SOC was treated non-perturbatively by solving the four-component Kohn–Sham–Dirac equation[41]. The density of states was calculated by applying the tetrahedron method. For all calculations, the appropriate experimental crystal structures were used. The bulk electronic structure calculations were carried out on a well-converged mesh of 27,000 k points ($30 \times 30 \times 30$ mesh, 2,496 points in the irreducible wedge of the Brillouin zone). The strong Coulomb repulsion in the Co $3d$ shell was taken into account in a mean-field way, applying the GGA + U approximation in the atomic-limit flavour, with $U = 4$ eV (ref. 22).

The surface electronic structure was calculated using a symmetric slab containing nine CoO_2 layers with Co in the centre, and separated by a vacuum gap of 15 Å along the z direction. The influence of including SOC in the calculations, which leads to spin-splitting of the surface states, is shown explicitly in Extended Data Fig. 3d. The layer-projected Co PDOS and the layer-resolved charge accumulation are shown in Extended Data Fig. 3c. A dense k mesh of $20 \times 20 \times 4$ points was used for the calculations. For this slab thickness the calculations are well converged with respect to the electronic states of the three central layers. However, owing to the slight off-stoichiometry of the slab, the partial charges of these layers are slightly modified from their true bulk values. We therefore set the Fermi level in the calculations to match the experimental crossing vectors of the surface states. However, this causes a small upward shift of the hole-like bands near $\overline{M}$, causing them to intersect the Fermi level in the slab calculation (Fig. 3e), contrary to the case for the true bulk electronic structure (Fig. 2b). We neglect these pockets in plotting the calculated Fermi surface (Fig. 3b). Supercell calculations were also performed for fully relaxed crystal structures, yielding qualitatively the same results as in the calculations performed for the ideal truncated bulk crystals used for the results presented here. The OAM shown in Fig. 3d and Extended Data Fig. 2 were calculated by downfolding the DFT supercell calculation (neglecting spin–orbit interactions) onto Wannier functions. SOC was added at the tight-binding level for these Wannier orbitals, enabling us to calculate the OAM of the surface states with and without SOC, as shown in Extended Data Fig. 2.

Tight binding models. To gain further understanding of the mechanism by which the difference in the on-site energy between the surface and subsurface oxygen stabilizes a giant ISB, ultimately leading to spin splitting of the full atomic SOC strength, we developed a minimal tight-binding model that describes the surface CoO_2 layer (see Fig. 4a, b). This model is broadly justified by the DFT supercell calculations, which indicate that the surface states are almost entirely localized in the topmost CoO_2 layer, and is described below.

A tight-binding Hamiltonian was constructed using the Slater–Koster parameterization of the energy integrals[42], in the cubic (xy, yz, $3z^2 - r^2$, xz, $x^2 - y^2$, $p1_y$, $p1_z$, $p1_x$, $p2_y$, $p2_z$, $p2_x$) basis, where $p1$ and $p2$ refer to the orbitals on the two

distinct oxygens, and the $\hat{z}$ axis is taken to be normal to the crystal surface. For illustrative purposes and maximum simplicity, in Extended Data Fig. 4 we retain only Co–O–Co hopping between Co t_{2g} and O p_z orbitals, which are dominant at the Fermi level, and neglect the small trigonal crystal field splitting of the t_{2g} levels. Better agreement with our DFT calculations can be obtained by including both in-plane O orbitals as well as direct Co d–d hopping (Extended Data Fig. 7).

Once the spin degree of freedom is taken into account the Hamiltonian is represented by a 22×22 matrix. It is a sum of three terms: the kinetic term H_K, the spin–orbit term H_{SO} and the crystal field term H_{CF}. The fact that the octahedral and crystallographic axes do not coincide (Fig. 4a) necessitates a coordinate transformation between cubic and trigonal orbital basis sets. Here we discuss all of the contributions to the total Hamiltonian, as well as the free parameters of the model.

The kinetic part of the Hamiltonian is constructed in the basis of cubic harmonics, with the $\hat{z}$ axis normal to the crystal surface. This choice of coordinate system makes it easy to evaluate directional cosines between neighbouring atoms: $l = \sin\theta\cos\phi$, $m = \sin\theta\sin\phi$ and $n = \cos\theta$, where θ and ϕ are the usual polar angles. The experimental crystal structure of $PtCoO_2$ (ref. 22), with the hexagonal lattice constants of $a = 2.82$ Å and $c = 17.8$ Å, and the Pt–O distance $z = 0.114c$, was used to determine the relative positions of the atoms. If the Co atom is placed at the origin, $(0, 0, 0)$, then the positions of two distinct oxygen atoms are given by $(1/2, 1/(2\sqrt{3}), 0.33)a$ and $(1/2, -1/(2\sqrt{3}), -0.33)a$. Extended Data Table 2 lists all of the hopping paths considered in the extended model, along with the angles between the nearest-neighbour atoms in the geometry outlined above, and the Slater–Koster parameters needed to describe the hopping[42].

The Co crystal field is diagonal in the trigonal basis, $(u_+, u_-, x_0, x_1, x_2)$, where u_+ and u_- are the two e_g^σ orbitals, x_0 is a_{1g}, and x_1 and x_2 are of e_g^π symmetry. The trigonal basis is related to the cubic one via the basis transformation[43] $(u_+, u_-, x_0, x_1, x_2) = B_{c \to t}(xy, yz, 3z^2 - r^2, xz, x^2 - y^2)$, where

$$B_{c \to t} = \frac{1}{\sqrt{6}} \begin{pmatrix} i & -\sqrt{2}i & 0 & -\sqrt{2} & -1 \\ i & -\sqrt{2}i & 0 & \sqrt{2} & 1 \\ 0 & 0 & \sqrt{6} & 0 & 0 \\ \sqrt{2}i & i & 0 & 1 & -\sqrt{2} \\ \sqrt{2}i & i & 0 & -1 & \sqrt{2} \end{pmatrix}$$

The coordinate transformation between the bases is then given by $T_{c \to t} = (B_{c \to t}^{-1})^T$, and the crystal field Hamiltonian in the cubic basis can be found using $H_{CF}^c = T_{c \to t}^{-1} H_{CF}^t T_{c \to t}$, where H_{CF}^t is the diagonal crystal field Hamiltonian in the trigonal basis. Allowing for both the octahedral (C_o) and trigonal (C_t) crystal field, H_{CF}^t is

$$H_{CF}^t = \begin{pmatrix} C_o & 0 & 0 & 0 & 0 \\ 0 & C_o & 0 & 0 & 0 \\ 0 & 0 & C_t & 0 & 0 \\ 0 & 0 & 0 & 0 & 0 \\ 0 & 0 & 0 & 0 & 0 \end{pmatrix}$$

In the maximally simplified model, called model I (Extended Data Fig. 4), the e_g^σ orbitals are completely neglected, which is achieved technically by applying a very large octahedral crystal field. An overall on-site energy E_{Co} is added to all of the Co states. The on-site energy of the in-plane and out-of-plane $2p$ orbitals of the first (second) oxygen are labelled E_1^{xy} and E_1^z (E_2^{xy} and E_2^z), respectively. In the simplified model I, which considers only the $p_{1,2}^z$ orbitals, large on-site energies $E_{1,2}^{xy}$ are applied.

The spin–orbit Hamiltonian is $H_{SO} = \xi \mathbf{L} \cdot \mathbf{S}$, where ξ is the atomic SOC constant of the Co $3d$ orbitals, taken to be 70 meV (ref. 26). The Hamiltonian in the cubic basis ($xy\downarrow$, $yz\downarrow$, $3z^2 - r^2\downarrow$, $xz\downarrow$, $x^2 - y^2\downarrow$, $xy\uparrow$, $yz\uparrow$, $3z^2 - r^2\uparrow$, $xz\uparrow$, $x^2 - y^2\uparrow$), where $\uparrow$ ($\downarrow$) denotes spin-up (spin-down), is

$$H_{SO} = \frac{\xi}{2} \begin{pmatrix} 0 & 0 & 0 & 0 & -2i & 0 & -1 & 0 & -i & 0 \\ 0 & 0 & 0 & -i & 0 & 1 & 0 & -\sqrt{3} & 0 & -i \\ 0 & 0 & 0 & 0 & 0 & 0 & \sqrt{3}i & 0 & \sqrt{3} & 0 \\ 0 & i & 0 & 0 & 0 & i & 0 & -\sqrt{3} & 0 & 1 \\ 2i & 0 & 0 & 0 & 0 & 0 & i & 0 & -1 & 0 \\ 0 & 1 & 0 & -i & 0 & 0 & 0 & 0 & 0 & 2i \\ -1 & 0 & -\sqrt{3}i & 0 & -i & 0 & 0 & 0 & i & 0 \\ 0 & -\sqrt{3} & 0 & \sqrt{3} & 0 & 0 & 0 & 0 & 0 & 0 \\ i & 0 & \sqrt{3} & 0 & -1 & 0 & -i & 0 & 0 & 0 \\ 0 & i & 0 & 1 & 0 & -2i & 0 & 0 & 0 & 0 \end{pmatrix}$$

The two sets of parameters used to calculate the tight-binding band structure are shown in Extended Data Table 3. Model I is maximally simplified, retaining only Co–O nearest-neighbour hopping between Co t_{2g} and O p_z orbitals as discussed above, to isolate the key ingredients necessary for the large ISB energy scale (Extended Data Fig. 4). Co–O hopping is parameterized using two Slater–Koster parameters, $V_{dp\sigma}$ and $V_{dp\pi}$, using the empirical relation $V_{dp\pi} = -\sqrt{3}/(4V_{dp\sigma})$ (ref. 44). The on-site energies of the oxygen p_z orbitals are estimated from the density of states shown in Extended Data Fig. 3, and chosen to be $E_{O2} = -7\,eV$ ($E_{O1} = -3.2\,eV$) for oxygen below (above) Co. Guided by the bandwidth and filling of the CoO_2-derived surface states from our DFT supercell calculations, the total bandwidth is required to be about 500 meV, and the Fermi level to be about 100 meV below the top of the band. This sets the on-site energy of the Co orbitals to be $-600\,meV$, and the hopping parameter $V_{dp\sigma}$ to 1.2 eV, a value similar to those obtained from fits to the DFT band structure of the related compound Na_xCoO_2 (ref. 45). The differences between the oxygen and Co on-site energies, which are relevant for determining effective hopping parameters, are $\Delta_{O1} = -2.6\,eV$ and $\Delta_{O2} = -6.4\,eV$. For the calculation with no asymmetry (Extended Data Fig. 4), the on-site energy difference was required to satisfy $2/\Delta_O = 1/\Delta_{O1} + 1/\Delta_{O2}$, yielding the oxygen on-site energy of $E_O = -4.3\,eV$.

A slightly more advanced model, called model II, additionally incorporates direct Co–Co and O–O hopping, as well as the full Co $3d$ and O $2p$ orbital manifolds. Because the in-plane oxygen orbitals do not directly participate in the Pt–O bonding, their on-site energy is allowed to be different to that of the p_z orbitals. In particular, the DFT PDOS suggests the difference between $E_1^{x,y}$ and $E_2^{x,y}$ is about 2 eV smaller than that between E_1^z and E_2^z. Allowing these different hopping paths, plausible for the real material, increases the degree of orbital mixing and therefore spin splitting, across k space. The calculated electronic structure for this model is shown in Extended Data Fig. 7.

Data availability. The data that underpin the findings of this study are available at http://dx.doi.org/10.17630/83be07cb-5ea6-47d3-8136-d75392da4a3d.

33. Shannon, R. D., Prewitt, C. T. & Rogers, D. B. Chemistry of noble metal oxides. II. Crystal structures of platinum cobalt dioxide, palladium cobalt dioxide, coppper iron dioxide, and silver iron dioxide. *Inorg. Chem.* **10,** 719–723 (1971).
34. Shannon, R. D., Rogers, D. B., Prewitt, C. T. & Gillson, J. L. Chemistry of noble metal oxides. III. Electrical transport properties and crystal chemistry of ABO₂ compounds with the delafossite structure. *Inorg. Chem.* **10,** 723–727 (1971).
35. Tanaka, M., Hasegawa, M. & Takei, H. Growth and anisotropic physical properties of PdCoO₂ single crystals. *J. Phys. Soc. Jpn* **65,** 3973–3977 (1996).
36. Sobota, J. A. *et al.* Electronic structure of the metallic antiferromagnet PdCrO₂ measured by angle-resolved photoemission spectroscopy. *Phys. Rev. B* **88,** 125109 (2013).
37. Bigi, C. *et al.* Very Efficient Spin Polarization Analysis (VESPA): new exchange scattering-based setup for spin-resolved ARPES at APE-NFFA beamline at Elettra. *J. Synchrotron Radiat.* **24,** 750–756 (2017).
38. Koepernik, K. & Eschrig, H. Full-potential nonorthogonal local-orbital minimum-basis band-structure scheme. *Phys. Rev. B* **59,** 1743–1757 (1999).
39. Opahle, I., Koepernik, K. & Eschrig, H. Full-potential band-structure calculation of iron pyrite. *Phys. Rev. B* **60,** 14035–14041 (1999).
40. Perdew, J. P., Burke, K. & Ernzerhof, M. Generalized gradient approximation made simple. *Phys. Rev. Lett.* **77,** 3865–3868 (1996).
41. Eschrig, H., Richter, M. & Opahle, I. in *Theoretical and Computational Chemistry* (ed. Schwerdtfeger, P.) Ch. 12, 723–776 (Elsevier, 2004).
42. Slater, J. C. & Koster, G. F. Simplified LCAO method for the periodic potential problem. *Phys. Rev.* **94,** 1498–1524 (1954).
43. Sugano, S., Tanabe, Y. & Kamimura, H. *Multiplets of Transition-Metal Ions in Crystals* (Academic Press, 1970).
44. Wu, W. B. *et al.* Orbital Symmetry and Electron Correlation in Na$_x$CoO₂. *Phys. Rev. Lett.* **94,** 146402 (2005).
45. Johannes, M. D., Papaconstantopoulos, D. A., Singh, D. J. & Mehl, M. J. A tight-binding investigation of the Na$_x$CoO₂ Fermi surface. *Europhys. Lett.* **68,** 433–439 (2004).
46. Park, J.-H., Kim, C. H., Rhim, J.-W. & Han, J. H. Orbital Rashba effect and its detection by circular dichroism angle-resolved photoemission spectroscopy. *Phys. Rev. B* **85,** 195401 (2012).
47. Koshibae, W. & Maekawa, S. Electronic state of a CoO₂ layer with hexagonal structure: a Kagomé lattice structure in a triangular lattice. *Phys. Rev. Lett.* **91,** 257003 (2003).
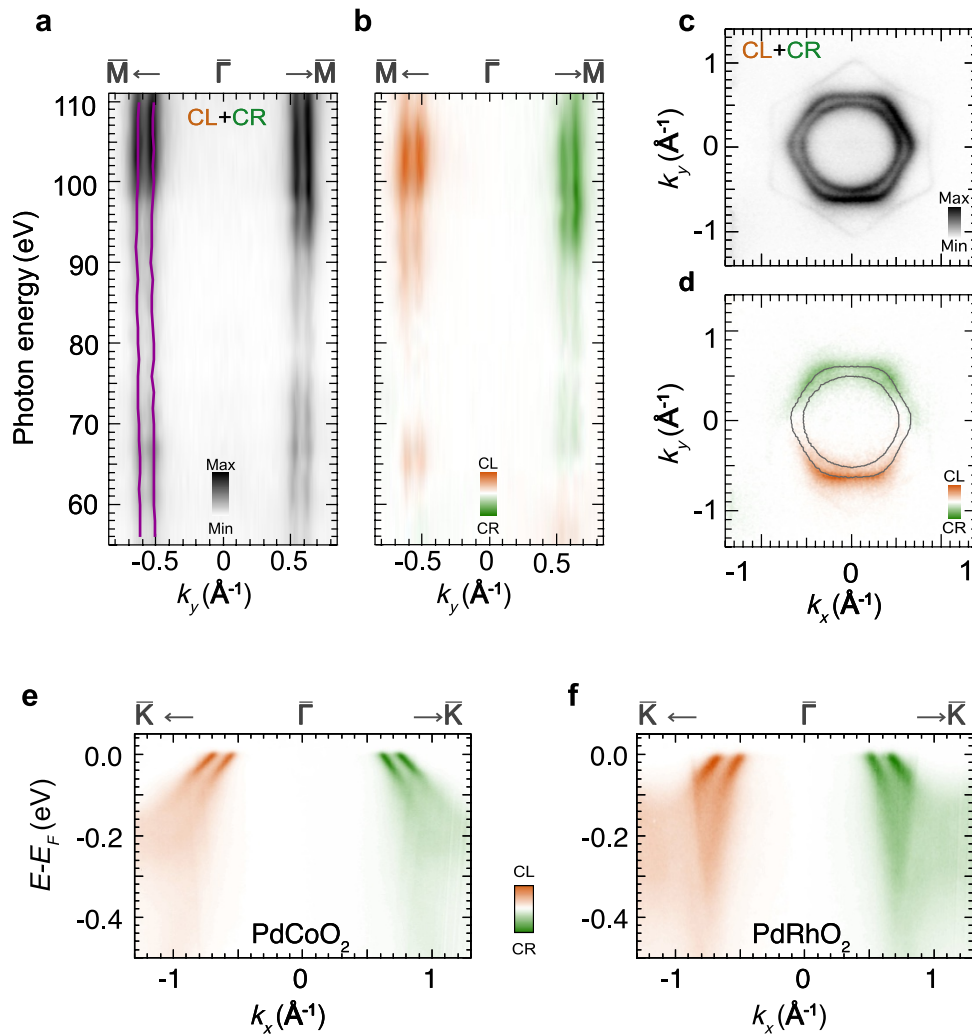
Extended Data Figure 1 | Photon energy and polarization dependent ARPES. a, The intensity at the Fermi level ($E_F \pm 5$ meV; sum of measurements with circularly left (CL)- and circularly right (CR)-polarized light), as a function of incident photon energy in $PtCoO_2$. The full purple lines correspond to the peak positions of fits to momentum distribution curves at the Fermi level. The Fermi crossing vectors do not depend on the photon energy, indicating that the states attributed to the CoO_2 surface layer are indeed two dimensional. **b–d**, A strong circular dichroism of these states is evident over an extended photon energy range

(**b**), and with an in-plane momentum dependence indicating the same chirality of OAM for the two spin-split bands (**d**; $h\nu = 110$ eV)[25,46]. The grey lines in **d** represent the Fermi momenta extracted from the sum of the measurements in CL and CR polarizations (**c**) by fitting momentum distribution curves radially around the Fermi surface. **e, f**, Similar to $PtCoO_2$, $PdCoO_2$ (**e**) and $PdRhO_2$ (**f**) surface states also show strong circular dichroism ($h\nu = 90$ eV) of the same sign on the two spin-split branches.

a Without SOC   **b** With SOC   **c** With SOC
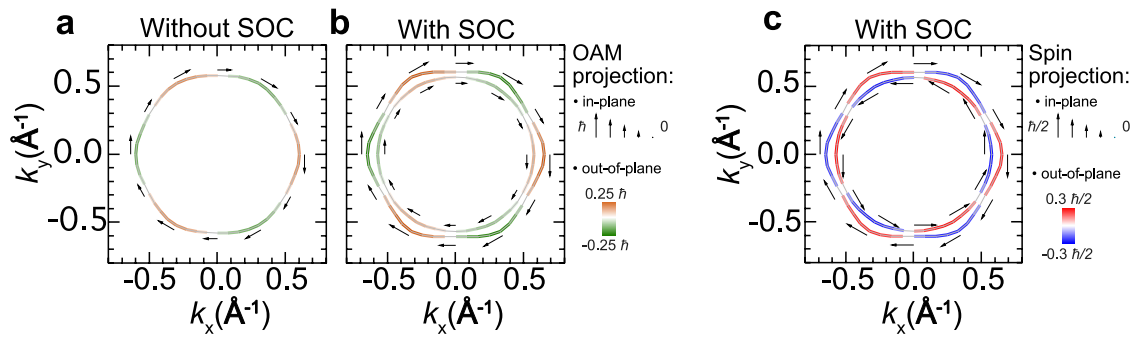
**Extended Data Figure 2 | OAM of CoO_2 surface states in $PtCoO_2$.**
a, Fermi surface of the surface states calculated without SOC, with arrows indicating the expected value of the in-plane OAM (see Methods) in the direction normal to the momentum and the colouring indicating a small out-of-plane OAM canting. The OAM develops as a result of the ISM even in the absence of SOC. **b**, Once SOC is included, the Fermi surface is split into two, both retaining the same OAM direction as in the no-SOC case. **c**, The two Fermi surfaces with the same OAM polarization carry opposite spin polarization, confirming that the surfaces states seen here are in the strong ISB limit (compare with Fig. 1).
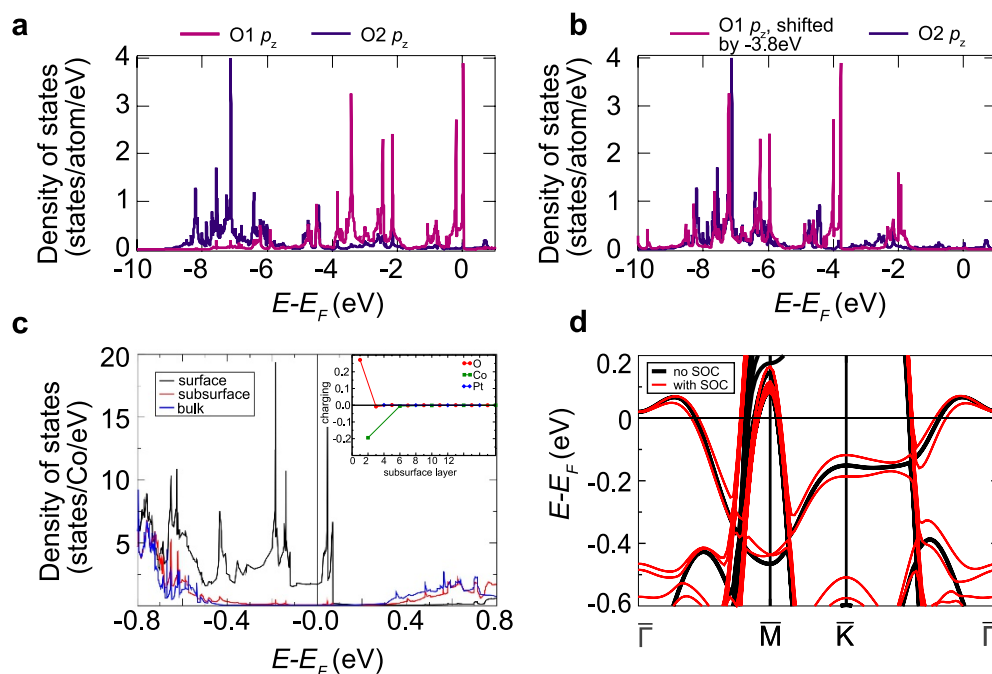
Extended Data Figure 3 | DFT supercell calculations. a, The oxygen p_z PDOS for layers above (O1, pink) and below (O2, purple) the Co layer. The p_z PDOS of O1 is much larger than that of O2 close to the Fermi level (see also Fig. 4c, d). **b**, Except for this added weight, the p_z PDOS of O1, shifted by -3.8 eV in binding energy, well approximates that of O2. **c**, Co PDOS near the Fermi level for different Co layers. The surface state between about -0.45 eV and 0.1 eV has very little contribution from Co atoms below the first layer. The PDOS of the subsurface Co atoms is almost bulk-like. This is also reflected by the charging of the surface shown in the inset.

The plot shows the additionally accumulated charge versus depth below the surface, referenced to the constituent bulk charges. Only the surface O layer and the topmost Co layer deviate substantially from the bulk. In particular, the pronounced difference (asymmetry) between the two O layers of the CoO_2 surface layer is very clearly demonstrated. Surface relaxation has only a minor effect on this scenario. **d**, Close-up of the band structure of $PtCoO_2$ around the Fermi level. For the narrow Co–O surface band (between about -0.45 eV and 0.1 eV), the SOC (red lines) leads to a spin splitting of this band, with only small changes to the dispersion.
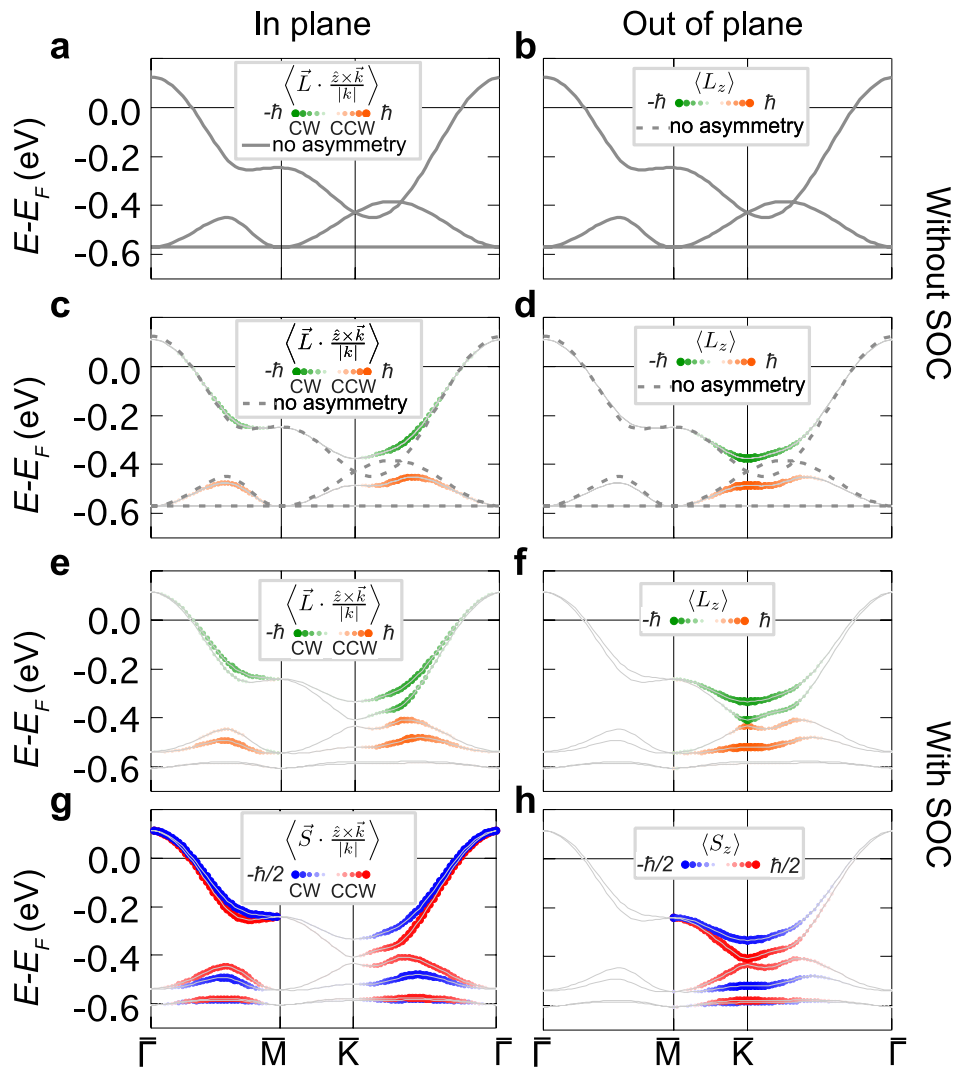
Extended Data Figure 4 | Development of OAM and SAM. a–h, The band structure obtained from a minimal tight-binding model (see Methods) reveals the key elements for maximal Rashba-like spin splitting. The calculations are shown without SOC or ISB (**a, b**), with ISB but no SOC (**c, d**), and with ISB and SOC (**e–h**). The chiral clockwise (CW) and anticlockwise (CCW) in-plane (**c, e**) and out-of-plane (**d, f**) OAM and chiral clockwise and anticlockwise in-plane (**g**) and out-of-plane (**h**) SAM are shown by colouring (see legends). If the two oxygens have the same on-site energy (no asymmetry, $E_{O1} = E_{O2}$), and neglecting SOC (**a, b**), then the electronic structure closely resembles that of a Kagome model, which has previously been used to describe the CoO_2 layer of Na_xCoO_2 (ref. 47): the lowest band is flat, and the other two bands cross at the Brillouin zone corner $\overline{K}$ and along the $\overline{\Gamma}-\overline{K}$ line, where hybridization is forbidden by symmetry. OAM is quenched in this inversion-symmetric environment. Introducing asymmetry as a result of a difference in the on-site energy of O1 and O2 (**c, d**) allows orbital mixing, and hybridization gaps open where there are crossings in the absence of the symmetry breaking. The orbital mixing enables these bands to develop a large (magnitude approaching $\hbar$) OAM even in the absence of SOC. This is largely chiral (OAM perpendicular to in-plane momentum) along the $\overline{\Gamma}-\overline{K}$ and $\overline{\Gamma}-\overline{M}$ directions, and crosses over to the OAM having a large out-of-plane component close

to $\overline{K}$ where any in-plane component must vanish owing to symmetry. For such an in-plane and out-of-plane OAM to develop there must be an out-of-plane and in-plane ISB, respectively. The fact that the asymmetric hopping occurs via the layers above and below Co naturally gives rise to the out-of-plane ISB. The opposite orientation of nearest-neighbour Co–O bonds to the oxygen layers above and below the transition-metal plane (Fig. 4b) additionally provides the in-plane ISB. Together, this enables the OAM to remain large across a greater portion of the Brillouin zone, rather than being suppressed in the broad vicinity of the $\overline{K}$ point. Crucially, the hybridization gaps between states of opposite OAM opened by such ISB are as large as 140 meV for the realistic parameters used here, about twice the size of atomic SOC. This difference in energy scales means that the spin–orbit interaction introduces an additional splitting between the states of spin that are parallel and antiparallel to the pre-existing OAM, which is itself not greatly altered (**e–h**). The energetic splitting assumes the full value of the atomic SOC, validating the simple schematic shown in Fig. 1b. This picture is consistent with our spin-resolved ARPES (Fig. 3c) and CD–ARPES (Extended Data Fig. 1 and Fig. 2d) data, which show that the two spin-split branches of the CoO_2-derived surface states host the same sign of OAM.
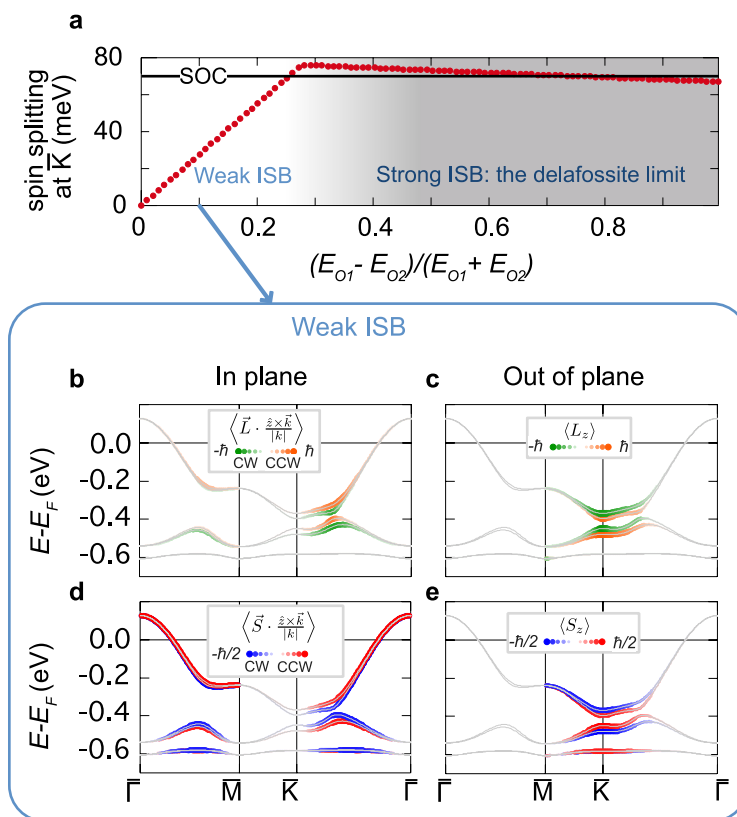
Extended Data Figure 5 | Crossover from weak to strong ISB. a, Spin splitting at the $\overline{K}$ point, calculated using our minimal single-layer tight-binding model for edge-sharing (TM)O_2 octahedra (Methods and Extended Data Tables 2 and 3), keeping the SOC strength fixed and varying the asymmetry of the upper and lower oxygen atoms, defined as $a = (E_{O1} - E_{O2})/(E_{O1} + E_{O2})$. Two regimes are clearly observed. When the ISB energy scale E_{ISB} is smaller than the SOC, spin splitting is proportional to, and limited by, E_{ISB} (weak ISB limit). Once E_{ISB} becomes dominant, the spin splitting saturates to a value that is limited by the spin–orbit energy scale, which is now weaker than E_{ISB} (strong ISB limit). **b–e**, To demonstrate that these two regimes correspond to the two limits illustrated in Fig. 1, we plot the band structure for $a = 0.1$, coloured by the chiral in-plane (**b**) and out-of-plane (**c**) OAM, and the chiral in-plane (**d**) and out-of-plane (**e**) spin. We find that the sign of the OAM switches between the two spin-split bands, in contrast to what is found in the strong ISB limit of the same model ($a = 0.4$, Extended Data Fig. 4e–h) and in the first-principles calculations for the surface states of PtCoO$_2$ (Extended Data Fig. 2b).
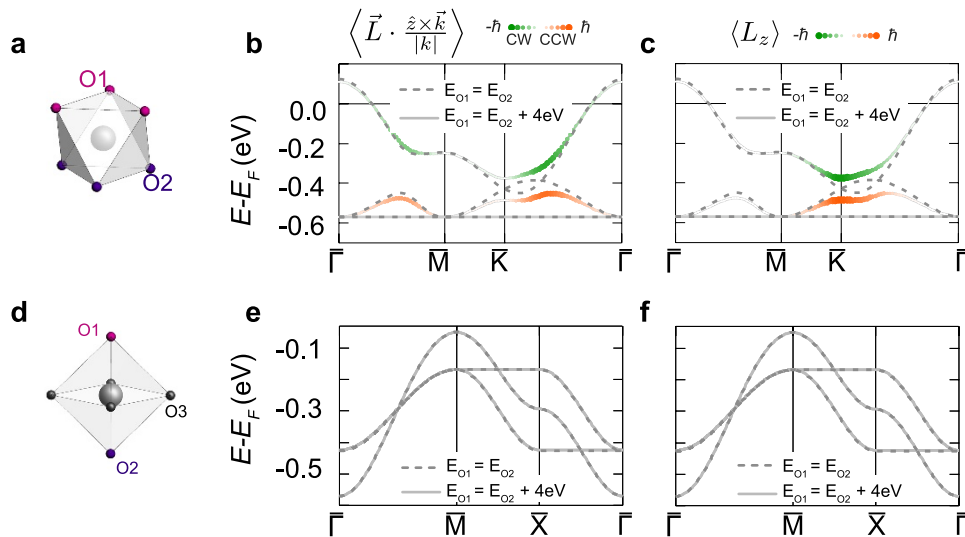
Extended Data Figure 6 | Comparison of surface on-site energy shifts for different structural configurations. a–f, To demonstrate the importance of the structural building blocks for the strength of ISB experienced by the relevant electrons, we compare the influence of surface on-site energy shifts on the edge-sharing transition-metal oxide layer found in delafossites (**a–c**) with that on its corner-sharing counterpart found in ⟨001⟩ perovskites (**d–f**). In both cases the breaking of covalent bonds at the surface can lead to an on-site energy shift of the surface oxygen (O1) with respect to subsurface oxygens. However, the influence on the spin splitting is very different. We use the same tight-binding model parameters for the two structures (as quoted in Extended Data Table 3), and in particular the same on-site energy shift, to calculate the bandstructure for a single transition-metal oxide layer. It is clear that, despite the same on-site energy shift at the surface, there is negligible effect on the band structure of the corner-sharing layer (**e, f**). This is because the dominant hopping path between transition-metal atoms is via the planar oxygen atoms (**a**), and so the relevant electrons do not feel this surface symmetry breaking strongly. Other mechanisms, such as surface distortions, are required to obtain a larger effect[29,30]. In contrast, for the delafossites, hopping between transition-metal atoms is via either the surface or subsurface oxygen layers (**a**), and so the effect of a pure on-site energy shift of the surface layer is already sufficient to drive a large OAM in the undistorted structure (**b, c**), as discussed in the main text.
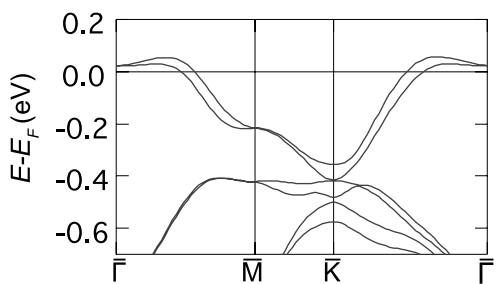
Extended Data Figure 7 | Tight binding model II. The band structure calculated using the tight-binding model II (see Extended Data Table 3). Additional hopping paths allowed in this model increase the orbital mixing, and thus the spin splitting, across *k* space.

Extended Data Table 1 | Comparison of the spin-split surface states of delafossite oxides

	$PtCoO_2$	$PdCoO_2$	$PdRhO_2$
m_1^*/m_e [$\overline{\Gamma}$-$\overline{M}$]	9.6 ± 0.5	7.9 ± 0.5	6 ± 1
m_2^*/m_e [$\overline{\Gamma}$-$\overline{M}$]	11.5 ± 0.8	10.1 ± 0.7	7 ± 1
m_1^*/m_e [$\overline{\Gamma}$-$\overline{K}$]	9.5 ± 0.5	9.0 ± 0.4	6.0 ± 0.5
m_2^*/m_e [$\overline{\Gamma}$-$\overline{K}$]	15 ± 1	16 ± 1	11 ± 1
Δk_F/ Å^{-1} [$\overline{\Gamma}$-$\overline{M}$]	0.11 ± 0.01	0.09 ± 0.01	0.13 ± 0.01
Δk_F/ Å^{-1} [$\overline{\Gamma}$-$\overline{K}$]	0.13 ± 0.01	0.12 ± 0.01	0.16 ± 0.01
ΔE/ meV [$\overline{K}$]	60	60	150

Quasiparticle masses m_i^* of the inner ($i=1$) and outer ($i=2$) surface bands, and spin splitting at the Fermi level Δk_F along the high-symmetry directions. These values are very similar for $PtCoO_2$ and $PdCoO_2$. Despite the lower masses for $PdRhO_2$, Δk_F is larger, as a consequence of the larger energetic splitting ΔE.

Extended Data Table 2 | Tight-binding model

Hopping path	θ	ϕ	SK parameters
Co-Co	90	30, 90, 150, 210, 270, 330	$V_{dd\sigma}, V_{dd\pi}, V_{dd\delta}$
Co-O1	60.08	0, 120, 240	$V_{dp\sigma}, V_{dp\pi}$
Co-O2	119.92	60, 180, 300	$V_{dp\sigma}, V_{dp\pi}$
O1-O1 (O2-O2)	90	30, 90, 150, 210, 270, 330	$V_{pp\sigma}, V_{pp\pi}$
O1-O2	139	30,150, 270	$V_{pp\sigma}, V_{pp\pi}$

The hopping paths considered in the tight binding model, angles (expressed in degrees) between nearest-neighbour atoms and relevant Slater–Koster (SK) parameters are shown.

Extended Data Table 3 | Tight-binding model parameterization

Parameter	Model I	Model II
$V_{dd\sigma}$	0	-0.3
$V_{dd\pi}$	0	0.15
$V_{dd\delta}$	0	0
$V_{dp\sigma}$	-1.2	-1.6
$V_{dp\pi}$	0.52	0.87
$V_{pp\sigma}$	0	0.5
$V_{pp\pi}$	0	-0.3
C_o	1000	1
C_t	0	0.5
E_1^z	-3.2	-3.2
E_2^z	-7	-7
$E_1^{x,y}$	1000	-4
$E_2^{x,y}$	1000	-6
E_{Co}	-0.57	-1.2
ξ	0.07	0.07

The parameters used in the two versions of the model (see Extended Data Figs 4 and 7 for models I and II, respectively), all expressed in electronvolts. The symbols are defined in Methods. The large values of 1,000 eV for on-site energies are used to effectively remove corresponding states from the model.